

CrossMark  
click for updatesCite this: *Chem. Sci.*, 2017, 8, 3489

# Novel bright-emission small-molecule NIR-II fluorophores for *in vivo* tumor imaging and image-guided surgery†

Yao Sun,<sup>‡ab</sup> Mingmin Ding,<sup>‡a</sup> Xiaodong Zeng,<sup>‡a</sup> Yuling Xiao,<sup>‡a</sup> Huaping Wu,<sup>a</sup> Hui Zhou,<sup>a</sup> Bingbing Ding,<sup>a</sup> Chunrong Qu,<sup>a</sup> Wei Hou,<sup>a</sup> AGA Er-bu,<sup>d</sup> Yejun Zhang,<sup>e</sup> Zhen Cheng<sup>c</sup> and Xuechuan Hong<sup>\*ad</sup>

Though high brightness and biocompatible small NIR-II dyes are highly desirable in clinical or translational cancer research, their fluorescent cores are relatively limited and their synthetic processes are somewhat complicated. Herein, we have explored the design and synthesis of novel NIR-II fluorescent materials (**H1**) without tedious chromatographic isolation with improved fluorescence performance (QY  $\approx$  2%) by introducing 2-amino 9,9-dialkyl-substituted fluorene as a donor into the backbone. Several types of water-soluble and biocompatible NIR-II probes: **SXH**, **SDH**, and **H1 NPs** were constructed *via* different chemical strategies based on **H1**, and then their potential to be used in *in vivo* tumor imaging and image-guided surgery in the NIR-II region was explored. High levels of uptake were obtained for both passive and active tumor targeting probes **SXH** and **SDH**. Furthermore, high resolution imaging of blood vessels on tumors and the whole body of living mice using **H1 NPs** for the first time has demonstrated precise NIR-II image-guided sentinel lymph node (SLN) surgery.

Received 18th January 2017  
Accepted 18th February 2017

DOI: 10.1039/c7sc00251c

rsc.li/chemical-science

## Introduction

As fluorescence imaging *in vivo* continues to gain increasing interest and expand within both academic and clinical settings, a transition shifted to longer wavelengths in the second near-infrared window (NIR-II, 1000–1700 nm) region could have clear-cut advantages of deeper tissue imaging, high spatial resolution, and high contrast owing to minimal auto-fluorescence and tissue scattering.<sup>1,2</sup> Improved imaging quality, superior lymphatic imaging, deeper brain tumor imaging, and higher tumor-to-background ratios have been achieved recently compared to the conventional NIR-I region (750–900 nm).<sup>3,4</sup> Developing novel NIR-II emitting agents for biomedical applications thus has high significance and directly promotes the field of biomedicine. Thus far, organic and

inorganic materials such as small molecules,<sup>5–7</sup> conjugated polymers,<sup>8</sup> carbon nanotubes,<sup>9,10</sup> quantum dots (QDs),<sup>11–13</sup> and rare earth nanoparticles,<sup>14,15</sup> have been actively employed for NIR-II fluorescence imaging.<sup>16</sup> However, reports of NIR-II fluorophores are still scarce and the small-molecule fluorescent cores are relatively limited compared with their NIR-I counterparts.<sup>6</sup> Hence, it prompts us to expand the library of small-molecule NIR-II fluorophores, which will significantly promote the widespread use of NIR-II imaging modality.

Several types of small-molecule NIR-II dyes with favorable excretion pharmacokinetics have been reported, in which the fluorophore units are generally composed of aromatic conjugate units based on a donor-acceptor-donor (D-A-D) structure with a benzobisthiadiazole (BBTD) core.<sup>5,6</sup> Among them, a small-molecule probe **Q4** was selected as a scaffold for the facile construction of NIR-II agent SCH1100 for targeted prostate cancer imaging.<sup>6,17</sup> However, the complexity and multiple synthetic steps with low yields, tedious chromatographic isolation and the weak brightness of **Q4** heavily hinder the wide application of such a promising agent in preclinical and clinical studies. Hence, many efforts should be made to simplify the synthetic strategy and optimize the brightness of small-molecule NIR-II fluorophores.

Herein, we report a novel small-molecule NIR-II dye **H1** with an improved synthetic protocol and fluorescence characteristics. At longer fluorescence emission wavelengths in the NIR-II region, the increased bandgap of molecular fluorophores generally gives way to reduce interactions between the

<sup>a</sup>State Key Laboratory of Virology, Key Laboratory of Combinatorial Biosynthesis and Drug Discovery (MOE), Hubei Provincial Key Laboratory of Developmentally Originated Disease, Wuhan University School of Pharmaceutical Sciences, Wuhan 430071, China. E-mail: xhy78@whu.edu.cn

<sup>b</sup>Key Laboratory of Pesticides and Chemical Biology, Ministry of Education, College of Chemistry, Central China Normal University, Wuhan 430079, China

<sup>c</sup>Molecular Imaging Program at Stanford (MIPS), Bio-X Program, Department of Radiology, Stanford University, California 94305-5344, USA

<sup>d</sup>Medical College, Tibet University, Lasa, 850000, China

<sup>e</sup>Suzhou NIR-Optics Technologies Co., Ltd, Suzhou, 215123, China

† Electronic supplementary information (ESI) available. See DOI: 10.1039/c7sc00251c

‡ These authors contributed equally to this work.

conjugated backbone and other molecules, causing a high fluorescence quantum yield (QY).<sup>18,19,20</sup> Therefore, in this work, R<sub>1</sub> substituent groups on the sp<sup>3</sup> carbon of the fluorene group are out-of-plane of the  $\pi$ -conjugated system and thus prevent intermolecular stacking that leads to fluorescence quenching. Meanwhile, newly introduced 2-amino 9,9-dialkyl-substituted fluorene moieties distort the BBTB backbone and thus effectively tune the electrostatic potential distribution and the bandgap to the desired range. Moreover, the fluorene moieties act as both the electron donor and protecting groups with the benefits of a compact molecular structure and shielding the backbone from aggregation (Fig. 1). Finally, three types of NIR-II probes (SXH, SDH, and H1 NPs) have been facily prepared according to the H1 scaffold, and demonstrated different biomedical applications such as passive/active tumor targeted imaging, high resolution imaging of blood vessels on tumors and the whole body, and image-guided sentinel lymph node surgery in the NIR-II imaging region. The novel organic fluorescent compound H1 provides unprecedented opportunities for the construction of a variety of NIR-II probes for *in vivo* molecular imaging.

## Results and discussion

As shown in Fig. 1, compound H1 was synthesized by a convergent route in 15% overall yield over 6 steps from commercially available starting materials without tedious chromatographic isolation (see ESI†). All compounds were characterized by NMR and ESI-MS, and also exhibited good solubility in common organic solvents such as CH<sub>2</sub>Cl<sub>2</sub> and THF (see ESI†). By modulating the non-resonant side chains of the carboxylic acid groups, the final NIR-II fluorophores could be systematically altered to tune the hydrophobicity, polarity and efficient conjugation of bio-targets. The UV-vis-NIR absorption band of H1 was at 600–1000 nm (in CH<sub>2</sub>Cl<sub>2</sub>) due to the formation of a strong charge-transfer structure between the D–A–D units (Fig. 2a). Meanwhile, the fluorescence emission spectrum of H1 was obtained and demonstrated a peak emission wavelength at ~1100 nm (Fig. 2a). The results indicated that the brightness of the fluorescence signals of H1 was superior to that of Q4 (Fig. 2b). Furthermore, the NIR-II signals of H1 were investigated under various LP filters (900–1400 nm) and no signals were observed with the 1300 nm and 1400 nm filters (Fig. 2c). H1 has exhibited high photo-stability compared to IR-26, with negligible decay under continuous excitation for 1 h (Fig. 2d).

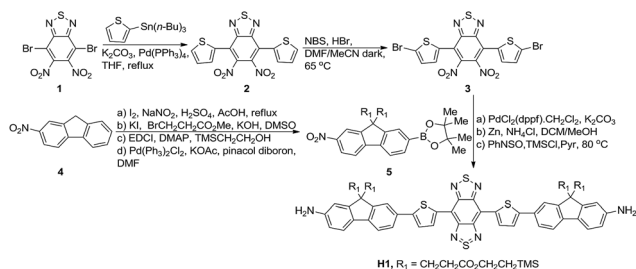


Fig. 1 Facile synthesis of compound H1.

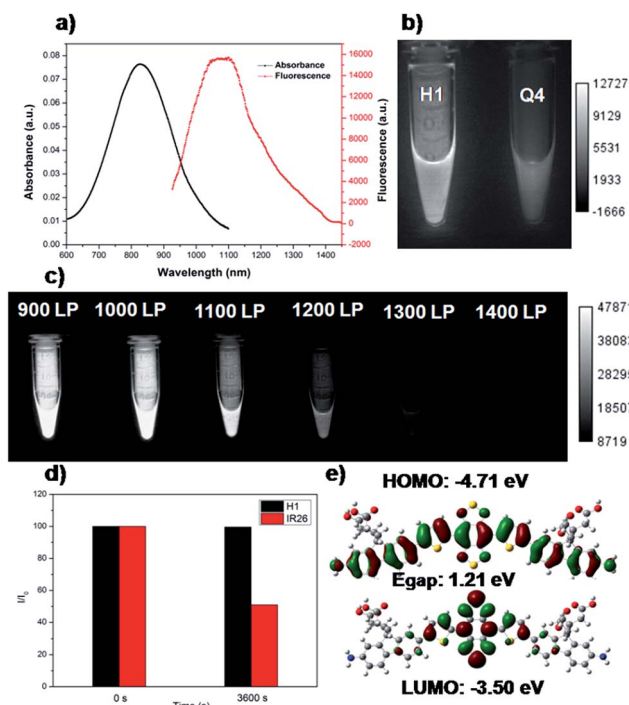


Fig. 2 (a) UV absorbance of H1 and NIR-II fluorescence emission of H1 with a peak at ~1100 nm under an 808 nm excitation laser (exposure time: 10 ms). (b) Comparison of NIR-II signals of H1 and Q4 under an 808 nm excitation laser (exposure time: 20 ms). (c) Comparison of NIR-II signals of H1 under various long-pass (LP) filters (900–1400 nm). (d) Comparison of the photo-stability of H1 and IR-26 in dichloromethane under continuous 808 nm excitation for 1 h. (e) HOMO and LUMO orbital surfaces of H1 using the DFT B3LYP/6-31G(d) scrf = (cpcm, solvent = CH<sub>2</sub>Cl<sub>2</sub>) method.  $E_{\text{gap}} = E_{\text{LUMO}} - E_{\text{HOMO}}$ .

The calculated HOMO and LUMO orbital surfaces of H1 have shown a larger band gap compared to that of Q4, leading to a higher performing fluorophore (Fig. 2e and Table S1†). The QY of H1 was ~2.0% under 785 nm excitation (in CH<sub>2</sub>Cl<sub>2</sub>, measured against an IR-26 reference with a nominal quantum yield of 0.5%, Fig. S1†). All these data demonstrated H1 could be a promising NIR-II dye, suitable for further NIR-II imaging applications.

SXH was easily prepared through conjugation of four carboxylic acid groups of H1 with PEG<sub>1000</sub> chains (Fig. 3a and ESI†). SXH was purified using HPLC and characterized using MALDI-TOF-MS (see ESI†). SXH exhibited high aqueous solubility and the fluorescence emission spectrum of SXH demonstrated a similar emission wavelength at ~1100 nm to that of H1 (Fig. 3b). The results from a cytotoxicity study further indicated the high viability of U87MG and L929 cells after 24 h of incubation with different doses of SXH (2, 4, 6, and 8  $\mu$ M), demonstrating the high biocompatibility of SXH (Fig. 3c). Excretion kinetics were investigated by intravenous injection of 100  $\mu$ g of SXH into U87MG tumor-bearing nude mice ( $n = 3$ ) for glioblastoma (GBM) imaging and collecting urine during the course of 24 h post-injection (P.I.). Glioblastoma, the most common primary brain tumor in adults, is usually rapidly fatal.<sup>21</sup> The care



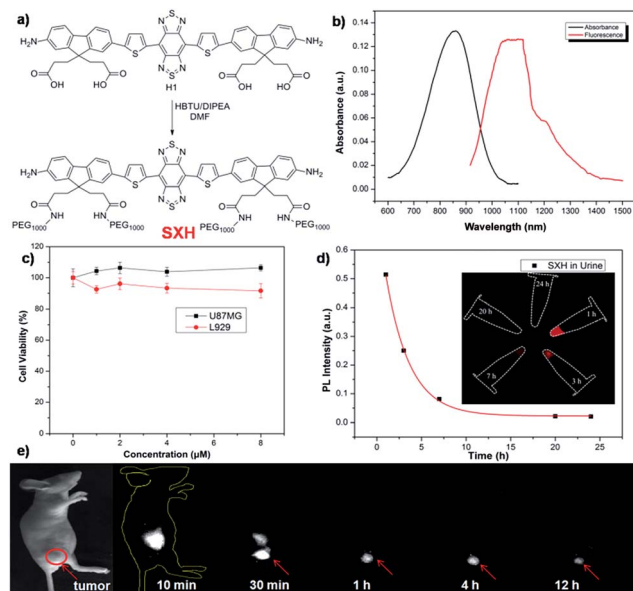


Fig. 3 (a) A schematic design of SXH showing four carboxylic acid groups of H1 conjugated with PEG<sub>1000</sub> chains. (b) UV absorbance of SXH and NIR-II fluorescence emission of SXH with a peak at ~1100 nm under an 808 nm excitation laser (solvents: water, exposure time: 10 ms). (c) Cellular toxicity of SXH with different doses (2, 4, 6, and 8 μM) in U87MG and L929 cells. (d) SXH agglomerated cumulative urine excretion curve during 24 h post-injection. (e) Non-specific targeting imaging of the U87MG tumor based on SXH under an 808 nm excitation (1000 LP and 200 ms).

for patients with a newly diagnosed glioblastoma entails surgical resection and concurrent radiation therapy (RT) and chemotherapy. Pharmacokinetics of SXH demonstrated rapid urine excretion, with ~90% of SXH removal through the renal system within the first few hours of the 24 h post-injection (Fig. 3d and Fig. S2†). Finally, U87MG tumor-bearing nude mice ( $n = 3$ ) were injected with 100 μg of SXH and non-invasive NIR-II fluorescence imaging of the glioblastoma tumor was conducted at particular time points. After 30 min post-injection, the tumor was clearly visible with a T/NT ratio of ~4 and showed passive uptake at all time points due to the non-specific diffusion and accumulation of SXH (Fig. 3e). *Ex vivo* biodistribution studies were further performed at 24 h post-injection of the probe to evaluate the distribution of SXH in major organs (Fig. S3†). It was found that SXH mainly accumulated in the kidneys, suggesting that the clearance route of SXH was through the renal system. In addition, a high level of accumulation was also observed in the tumor, indicating that SXH can passively target tumors and be used for future cancer theranostic applications (Fig. S3†).

Although PEGylation of H1 provided a rapidly excreted, versatile contrast agent capable of passive tumor uptake, H1 could provide more tumor-specific targeting by linking to a molecular imaging ligand. We next demonstrated the application of H1 for receptor-targeted glioma imaging. Integrin  $\alpha_v\beta_3$  has high expression levels in several malignant diseases including glioblastoma and are established biomarkers for metastatic diseases.<sup>22</sup> The integrin targeting peptide RGD

(arginine-glycine-aspartic acid) has shown promising results for non-invasive molecular imaging of integrin  $\alpha_v\beta_3$  expression in the NIR-I region.<sup>23</sup> Considering the advantages of NIR-II imaging, a novel integrin  $\alpha_v\beta_3$ -targeted NIR-II fluorophore, SDH, was developed and explored to investigate its imaging properties *in vivo*. SDH was prepared through conjugation of H1 with a mono-c(RGDfk) targeting peptide (Fig. 4a), and then purified by HPLC and characterized by MALDI-TOF [calcd for C<sub>72</sub>H<sub>79</sub>N<sub>15</sub>O<sub>14</sub>S<sub>4</sub>: 1589.481, found:  $m/z$  1589.669]. The fluorescence emission spectrum of SDH demonstrates an emission wavelength at ~1050 nm (Fig. 4b). The cell toxicity study also indicated the high biocompatibility of SDH *in vitro* (U87MG and L929 cells after 24 h incubation with 2, 4, 6, and 8 μM doses of SDH, Fig. S4†). These results demonstrated that SDH, as a promising and biocompatible NIR-II fluorescent probe, is suitable for tumor targeting imaging.

SDH was then intravenously injected (100 μg) into U87MG tumor-bearing mice ( $n = 3$  per group). From NIR-II imaging data, the U87MG tumor could be clearly visualized from the surrounding background tissue during 24–72 h post-injection (P.I.) (Fig. 4d, 1000LP, 200 ms), and the tumor uptake reached a maximum at 48 h. The specificity of SDH for integrin  $\alpha_v\beta_3$  was confirmed by the blocking experiment. The tumors fluorescence signals were successfully reduced at all time points after co-injection of RGD peptide (500 μg) with SDH for NIR-II imaging (Fig. 4d). An *ex vivo* biodistribution study indicated that high accumulation was observed in the liver and kidneys, which suggested that the clearance routes of SDH were through both hepatobiliary and renal systems (Fig. S5†). In addition, the uptake of SDH in tumors was far beyond that of other normal organs and no uptake could be observed in the blocking group,

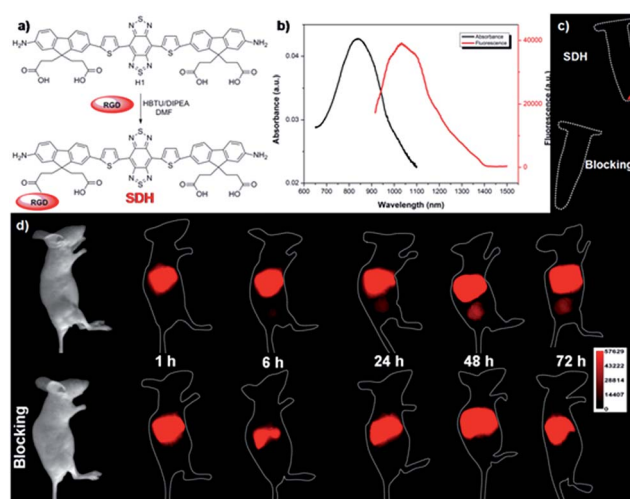


Fig. 4 (a) A schematic of SDH showing one of the carboxylic acid groups of H1 conjugated with targeted ligand RGD peptide. (b) UV absorbance and NIR-II fluorescence emission of SDH. (c) NIR-II signals of U87MG cell labelling by SDH and SDH + excess RGD as a blocking agent (block group) under 808 nm excitation (1000LP and 100 ms). (d) NIR-II images of U87MG tumor mice ( $n = 3$ ) at different time points (1, 6, 24, 48, and 72 h) after tail vein injection of SDH with or without the blocking agent RGD (500 μg) under 808 nm excitation (1000LP and 200 ms).



which further confirmed the good integrin  $\alpha_v\beta_3$ -targeted ability and specificity of **SDH** (Fig. S5 and S6†). Hence, the excellent translation ability of **SDH** represents a highly promising fluorescent probe for non-invasive monitoring of early stage glioblastoma in the NIR-II region.

An emerging fluorescence imaging application of NIR fluorophores, such as indocyanine green (ICG), is currently undergoing clinical trials in detecting sentinel lymph nodes (SLNs) for surgical resection.<sup>24</sup> Selectively removing sentinel lymph nodes alleviates lymphedema and other ailments that would be caused by total lymph node removal, which is performed to prevent cancer metastasis. Recent advances in NIR-I fluorescence molecular imaging (FMI) for intraoperative image-guided cancer resection have introduced new frontiers for FMI-based therapeutic interventions in preclinical research and clinical applications. The inherent advantages of this novel technology compared to bright light surgery, such as its high sensitivity, high superficial resolution, low cost, and real-time imaging capacity, have stimulated the development of fluorescent probes with different molecular features.<sup>25–33</sup> To demonstrate the feasibility of **H1** for SLN surgery, **H1** was encapsulated into a PEGylated surfactant, DSPE-mPEG<sub>5000</sub>, to prepare water-soluble and biocompatible NIR-II nanoprobes, **H1 NPs** (Fig. 5a). The prepared **H1 NPs** showed high monodispersity and homogeneity with an average particle size of  $\sim 70.0$  nm by transmission electron microscopy (TEM, Fig. 5b) and a hydrodynamic diameter of  $\sim 80.0$  nm as determined by dynamic light scattering (DLS, Fig. S7†). The fluorescence emission wavelength of **H1 NPs** was  $\sim 1100$  nm (Fig. S8†). The result of the cytotoxicity study indicated the high biocompatibility of **H1 NPs**

(Fig. S9†). The amount of **H1** encapsulated in the liposomes was measured by a UV/VIS spectrophotometer at 874 nm (ESI†). The dye encapsulation efficiency of **H1 NPs** was  $79.8 \pm 0.6\%$  ( $n = 3$ ).

The U87MG tumor-bearing nude mice ( $n = 3$ ) were injected with 150  $\mu$ L of **H1 NPs**. Immediately after injection, the superior imaging of blood vessels of the whole body and tumor could be clearly observed from the surrounding background tissue using NIR-II imaging (Fig. 5c). Based on this promising result, we applied **H1 NPs** for lymph node imaging and image-guided surgery on the C57BL/6J model (Fig. 5d). C57BL/6J mice were injected with 100  $\mu$ L of **H1 NPs**, with the help of NIR-II imaging, a SLN was successfully determined, even covered with soft tissue. After the SLN was exposed, it was then resected thoroughly. More importantly, the border of the SLN was easily distinguished, avoiding unnecessary damage of surrounding tissue such as nerves, vessels and tendons.

## Conclusions

In summary, we have developed a newly designed and facilely prepared NIR-II fluorophore **H1** with improved fluorescence by introducing 2-amino 9,9-dialkyl-substituted fluorene as a donor into the backbone. Based on this **H1** scaffold, three types of NIR-II imaging probe, **SXH**, **SDH** and **H1 NPs**, have been prepared and allow for integrin  $\alpha_v\beta_3$ -targeted glioma imaging. To the best of our knowledge, this is the first time that a NIR-II molecular fluorophore has been shown to delineate tumours from surrounding normal tissue. Various biomedical applications such as high resolution imaging of blood vessels on tumours and the whole body of living mice using **H1 NPs** were also performed through a passive targeted probe. With the help of NIR-II imaging, an SLN was successfully determined and resected thoroughly. Future work will focus on performing intraoperative image-guided cancer surgery in orthotopic models and specialized pharmacokinetic studies with the eventual goal of initiating clinical trials with a NIR-II small-molecule fluorophore.

## Acknowledgements

This work was partially supported by NSFC (81573383, 21390402, 81301268), NSFHP (2014CFB704), IS&TCPC (2015DFA30440, 2014CFB30020), the Major Project of Technology Innovation Program of Hubei Province (2016ACA126), the Applied Basic Research Programs of Scientific and Technologic Council of Suzhou (SYG201521), the Natural Science Foundation of Jiangsu Province (BK20160387), Beijing Nova Plan Z (131107000413063), and the Fundamental Research Funds for the Central Universities.

## Notes and references

- G. S. Hong, A. L. Antaris and H. J. Dai, *Nat. Biomed. Eng.*, 2017, **1**, 0010.
- G. S. Hong, J. C. Lee, J. T. Robinson, U. Raaz, L. M. Xie, N. F. Huang, J. P. Cooke and H. J. Dai, *Nat. Med.*, 2012, **18**, 1841–1846.

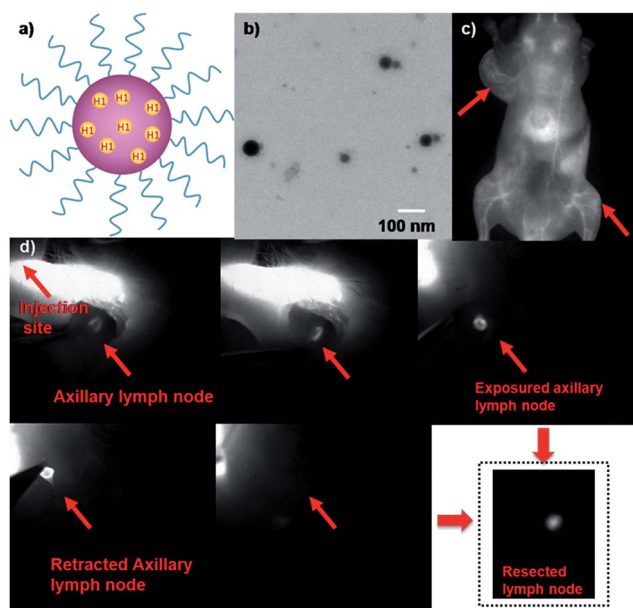


Fig. 5 (a) A schematic of **H1 NPs** showing the **H1** core and a hydrophilic PEG shell. (b) The TEM image of **H1 NPs**. (c) The NIR-II image of the blood vessels of the whole body and U87MG tumors after tail vein injection of **H1 NPs** under 808 nm excitation, 1000 LP and 100 ms; red arrows indicate the tumor. (d) NIR-II imaging-guided sentinel lymph node surgery on the C57BL/6J model (1000LP and 200 ms).



- 3 G. S. Hong, S. Diao, A. L. Antaris and H. J. Dai, *Chem. Rev.*, 2015, **115**, 10816–10906.
- 4 C. Y. Li, Y. J. Zhang, M. Wang, Y. Zhang, G. C. Chen, L. Li, D. M. Wu and Q. B. Wang, *Biomaterials*, 2014, **35**, 393–400.
- 5 A. L. Antaris, H. Chen, K. Cheng, Y. Sun, G. S. Hong, C. R. Qu, S. Diao, Z. X. Deng, X. M. Hu, B. Zhang, X. D. Zhang, O. K. Yaghi, Z. R. Alamparambil, X. C. Hong, Z. Cheng and H. J. Dai, *Nat. Mater.*, 2016, **15**, 235–242.
- 6 Y. Sun, C. Q. Rong, H. Chen, M. M. He, C. Tang, K. Q. Shou, S. Hong, M. Yang, Y. X. Jiang, B. B. Ding, Y. L. Xiao, L. Xing, X. C. Hong and Z. Cheng, *Chem. Sci.*, 2016, **7**, 6203–6207.
- 7 W. H. Zhu, *Sci. China: Chem.*, 2016, **59**, 203–204.
- 8 G. S. Hong, Y. P. Zhou, A. L. Antaris, S. Diao, D. Wu, K. Cheng, X. D. Zhang, C. X. Chen, B. Liu, Y. H. He, J. Z. Wu, J. Yuan, B. Zhang, Z. M. Tao, C. Fukunaga and H. J. Dai, *Nat. Commun.*, 2014, **5**, 4206.
- 9 G. S. Hong, S. Diao, J. L. Chang, A. L. Antaris, C. X. Chen, B. Zhang, S. Zhao, D. N. Atochin, P. L. Huang, K. I. Andreasson, C. J. Kuo and H. J. Dai, *Nat. Photonics*, 2014, **8**, 723–730.
- 10 S. Diao, J. L. Blackburn, G. S. Hong, A. L. Antaris, J. L. Chang, J. Z. Wu, B. Zhang, K. Cheng, C. J. Kuo and H. J. Dai, *Angew. Chem., Int. Ed.*, 2015, **54**, 14758–14762.
- 11 Y. Zhang, G. S. Hong, Y. J. Zhang, G. C. Chen, F. Li, H. J. Dai and Q. B. Wang, *ACS Nano*, 2012, **6**, 3695–3702.
- 12 G. S. Hong, J. T. Robinson, Y. J. Zhang, S. Diao, A. L. Antaris, Q. B. Wang and H. J. Dai, *Angew. Chem., Int. Ed.*, 2012, **51**, 9818–9821.
- 13 G. C. Chen, F. Tian, C. Y. Li, Y. J. Zhang, Z. Weng, Y. Zhang and Q. B. Wang, *Biomaterials*, 2015, **53**, 265–273.
- 14 D. J. Naczynski, M. C. Tian, M. Zevon, B. Wall, J. Kohl, A. Kulesa, S. Chen, C. M. Roth, R. E. Riman and P. V. Moqhe, *Nat. Commun.*, 2013, **4**, 2199.
- 15 X. Y. Jiang, C. Cao, W. Feng and F. Y. Li, *J. Mater. Chem. B*, 2016, **4**, 87–95.
- 16 X. N. Dang, L. Gu, J. F. Qi, S. Correa, G. R. Zhang, A. M. Belcher and P. T. Hammond, *Proc. Natl. Acad. Sci. U. S. A.*, 2016, **113**, 5179–5184.
- 17 Y. Sun, X. Ma, Z. Zhang, Z. Y. Sun, M. Loft, B. B. Ding, C. H. Liu, L. Y. Xu, M. Yang, Y. X. Jiang, J. F. Liu, Y. L. Xiao, Z. Cheng and X. C. Hong, *Bioconjugate Chem.*, 2016, **27**, 1857–1864.
- 18 G. Qian, Z. Zhong, M. Luo, D. B. Yu, Z. Q. Zhang, Z. Y. Wang and D. G. Ma, *Adv. Mater.*, 2009, **21**, 111–116.
- 19 G. Qian, J. P. Gao and Z. Y. Wang, *Chem. Commun.*, 2012, **48**, 6426–6428.
- 20 X. D. Zhang, H. Wang, A. L. Antaris, L. I. Li, S. Diao, R. Ma, A. Nguyen, G. S. Hong, Z. R. Ma, J. Wang, S. J. Zhu, J. M. Castellano, T. Wyss-Coray, Y. Y. Liang, J. Luo and H. J. Dai, *Adv. Mater.*, 2016, **28**, 6872–6879.
- 21 R. Stupp, *et al.*, *N. Engl. J. Med.*, 2005, **352**, 987–996.
- 22 M. Pfaff, K. Tangemann, B. Muller, M. Gurrath, G. Muller, H. Kessler, R. Timpl and J. Engel, *J. Biol. Chem.*, 1994, **269**, 20233–20238.
- 23 Y. Sun, X. Ma, K. Cheng, B. Wu, J. Duan, H. Chen, L. Bu, R. Zhang, X. Hu, Z. Deng, L. Xing, X. Hong and Z. Cheng, *Angew. Chem., Int. Ed.*, 2015, **54**, 5981–5984.
- 24 E. Tanaka, H. S. Choi, H. Fujii, M. G. Bawendi and J. V. Frangioni, *Ann. Surg. Oncol.*, 2006, **13**, 1671–1681.
- 25 M. Momiyama, Y. Hiroshima, A. Suetsugu, Y. Tome, S. Mii, S. Yano, M. Bouvet, T. Chishima, I. Endo and R. M. Hoffman, *Anticancer Res.*, 2013, **33**, 107–112.
- 26 R. M. Hoffman, *Invest. New Drugs*, 1999, **17**, 343–359.
- 27 R. M. Hoffman, *Nat. Rev. Cancer*, 2015, **15**, 451–452.
- 28 R. M. Hoffman and M. Yang, *Nat. Protoc.*, 2006, **1**, 1429–1438.
- 29 C. A. Metildi, S. Kaushal, C. R. Hardamon, C. S. Snyder, M. Pu, K. S. Messer, M. A. Talamini, R. M. Hoffman and M. Bouvet, *J. Am. Coll. Surg.*, 2012, **215**, 126–135.
- 30 C. A. Metildi, S. Kaushal, M. Pu, K. A. Messer, G. A. Luiken, A. R. Moossa, R. M. Hoffman and M. Bouvet, *Ann. Surg. Oncol.*, 2014, **21**, 1405–1411.
- 31 C. A. Metildi, S. Kaushal, C. S. Snyder, R. M. Hoffman and M. Bouvet, *J. Surg. Res.*, 2013, **179**, 87–93.
- 32 T. Murakami, Y. Hiroshima, Y. Zhang, M. Bouvet, T. Chishima, K. Tanaka, I. Endo and R. M. Hoffman, *J. Surg. Oncol.*, 2015, **112**, 119–124.
- 33 Y. Hiroshima, A. Maawy, Y. Zhang, S. Sato, T. Murakami, M. Yamamoto, F. Uehara, S. Miwa, S. Yano, M. Momiyama, T. Chishima, K. Tanaka, M. Bouvet, I. Endo and R. M. Hoffman, *PLoS One*, 2014, **9**, e99977.

